Laminar Boundary-Layer Instabilities on Hypersonic Cones: Computations for Benchmark Experiments

AIAA Paper 2005-5024, Presented at the 35th Fluid Dynamics Conference, Toronto, June 2005

Tyler W. Robarge* and Steven P. Schneider†

School of Aeronautics and Astronautics, Purdue University

West Lafayette, IN 47907-1282

ABSTRACT

Although significant advances have been made in hypersonic boundary-layer transition prediction in the last several decades, most design work still relies on empirical correlations or wind tunnel tests. Codes using the semi-empirical e^N method will need to be verified and validated before being used for expensive flight vehicles. The STABL code package and its PSE-Chem stability solver are used to compute first and second mode instabilities for both sharp and blunt cones at wind tunnel conditions, with laminar mean flows provided by the DPLR2D Navier-Stokes code. Stetson's 3.81 mm blunt cone case, a sharp cone at Mach 3.5, and a very blunt cone at Mach 8 are analyzed. The computed transition locations agree well with previous computations by other researchers, but larger differences are seen in the local amplification rates for the Stetson blunt cone case. The applicability of various transport property models and their effect on boundary layer stability are examined. This work helps to extend the applicability of STABL to low-temperature flows.

NOMENCLATURE

C_v	Specific heat at constant volume
E	disturbance kinetic energy
e_v	vibrational energy
k	thermal conductivity
M	Mach number; molecular weight
p	pressure
$Re_{\infty,s}$	Reynolds number $Re = \frac{U_\infty s}{\nu_\infty}$
r_n	nose radius
s	arc length along the body surface
T	temperature

t	time
u,v,w	velocity in x,y,z directions
x	distance in streamwise direction
y	distance in body-normal direction
z	distance in spanwise direction
α	streamwise complex wavenumber
β	spanwise complex wavenumber
μ	first coefficient of viscosity
ν	kinematic viscosity
ρ	density
σ	disturbance growth rate
ϕ	vector of disturbance quantities
ξ	streamwise computational coordinate
ψ	shape function; wave angle
Ω	domain of integration for PSE
ω	frequency

Superscripts

−	mean component
^	fluctuating component

Subscripts

i	imaginary; body-parallel direction
j	body-normal direction
o	stagnation; critical location
rot	component of the rotational mode
s	specific chemical species
tr	translational; transition
vib	vibrational
∞	freestream conditions

---

*1Lt, USAF and Hertz Fellow. Student Member, AIAA

†Professor. Associate Fellow, AIAA

[1]This paper is declared a work of the U.S. Government and is not subject to copyright protection in the United States.

INTRODUCTION

Despite more than fifty years of hypersonics research, many critical areas are still poorly understood [1]. Hypersonic flight remains a top priority in defense research, as any vehicle that ascends to or from space must traverse the hypersonic regime. The reduction in forward deployed forces since the

1

20050614 035

end of the Cold War has increased the need for hypersonics, as a need remains to be able to strike high-value, time-critical targets anywhere in the world in minutes or hours [2]. Hypersonic flight is a key component of most plans to provide that capability.

The location and extent of laminar to turbulent boundary-layer transition is a critical parameter in hypersonic vehicle design [1]. The transition location directly affects estimates of aeroheating and skin friction drag, which in turn affect heat shield weight and materials, range, and payload capacity. Vehicle designers can now compute the laminar and turbulent aeroheating with good accuracy; in many cases, the largest uncertainty in calculating the total heat flux to the vehicle results from the estimates of transition location [3].

Transition Prediction Methods

Transition prediction for vehicle design has historically relied on empirical correlations and extrapolations from wind tunnel experiments. Many correlations exist, and most fit some subset of the experimental data. However, no empirical model can accurately predict transition for a general dataset [1]. In fact, Schneider [4] has shown that for a general data set the predictions generated by different correlations scatter by a factor of three in momentum thickness Reynolds number and an order of magnitude in arc length Reynolds number. Extrapolating from wind tunnel experiments is also problematic. Any single ground facility can only match a small subset of the dozens of parameters that affect transition [5]. Further complicating matters, the accoustic noise produced by the turbulent boundary-layer on the walls of conventional hypersonic wind tunnels produces a freestream disturbance environment markedly different from that of flight. These disturbances have been shown to affect not only the transition location, but also the parametric trends [6]. This has led to a push for the development of 'quiet' tunnels, but there are currently no hypersonic wind tunnels that are quiet at significant Reynolds numbers anywhere in the world [7]. Flight tests can replicate all of the relevant parameters, but only limited information is available, and its expense is normally prohibitive.

Linear Stability Theory (LST) [8] and the Parabolized Stability Equations (PSE) [9] have been coupled with the semi-empirical e^N method to predict hypersonic transition on simple geometries. Recently, Malik [10] showed that transition locations could be correlated on two hypersonic flight tests using the PSE for chemically reacting flows and the e^N method. Although these methods have shown

success in research settings and in design for subsonic and transonic applications, hypersonic vehicle designers are hesitant to stake expensive programs on these newer methods until they have been shown to be better validated and simpler to use [11].

Since hypersonic vehicles remain a priority, and current design methods are inadequate, an improved method for hypersonic boundary-layer transition prediction is needed. The overall project that this work is a part of aims to provide mechanism-based methods that are suitable for design purposes, including predictions using the PSE and the e^N method. This will not be the final solution to the problem of transition prediction. However, it is hoped that the inclusion of more of the relevant flow physics will result in a more accurate and more robust method than those which are currently in use. The present work is concerned primarily with the verification and validation of the 2D/axisymmetric version of PSE/e^N code package.

Verification and Validation

Before computational results can be used to make important decisions, measures must be taken to ensure confidence in the accuracy of the predictions. Although this issue has received considerable attention in recent years, developments in this area have not kept pace with increases in code size and complexity and the increasing reliance on computations to reduce the number and scope of wind tunnel and flight test cases [12].

Blottner [13] defines code validation as solving the right governing equations and code verification as solving the governing equations right. Examples of validation include confirming the applicability of the assumptions made and comparing the accuracy of the closure models throughout the relevant parameter space. Verification means evaluating the accuracy of the numerical procedures used to solve the governing equations. Examples of verification include checking for general programming errors and ensuring that results are converged and grid independent. Code validation can only be accomplished by detailed comparisons to experimental data [14], and the validation of applicable equations and models is a responsibility of the community at large. In general, a code must be verified before it can be fully validated. For this reason, this work will focus primarily on verification, although the validation of the transport properties will be discussed.

Several approaches exist for code verification, including grid refinement studies, varying the boundary conditions, solving problems that have an analytical solution, and comparing results with previ-

ously verified codes [12,14]. Grid refinement studies and comparisons with other codes will be used in the present effort. This work expands on previous verification and validation by Johnson and Johnson et al. [15–18]. Additional details about the work presented here are in Robarge [19].

CODE DESCRIPTION

The computations presented in this paper were performed using the STABL code package. STABL is designed to be a comprehensive boundary-layer stability analysis and transition prediction tool, and it includes a mean flow code, a stability code, and other utilities such as a Graphical User Interface (GUI) and a grid generator. STABL is modular in nature, allowing individual components to be used instead of the whole package. Further details about STABL and its components can be found in Johnson and Candler [18] and Robarge [19].

The laminar mean flows were obtained using the code DPLR2D, which solves the axisymmetric Navier-Stokes equations using the Data Parallel Line Relaxation (DPLR) method [20] with modified Steger-Warming flux vector splitting [21]. The solver is second order accurate in both the streamwise and wall-normal directions, although it drops to first order accuracy near the shock. DPLR2D and the PSE-Chem stability code can both handle a range of real gas effects, including perfect gas or reacting flows with chemical non-equilibrium using a general set of chemical reactions. Thermal non-equilibrium is treated using a two-temperature model with both translational and vibrational modes. Chemical and thermal equilibrium can both be simulated through large relaxation rates.

The grids used for the mean flow solutions were created using the grid generator included with STABL. The model surface and outer boundaries were each specified using a single arc section and one or more line segments. In the case of a sharp cone, only line segments were used. The outer boundary was specified so as to closely match the local shock angle. The lines of constant i were constrained to be always normal to the wall. The surface spacing was uniform on the nose, and exponential stretching using multiple segments distributed points smoothly on the cone frusta. The lines of constant j were constructed by interpolating between spacings specified at the upstream and downstream boundaries. Exponential stretching was used to cluster points within the boundary-layer. Experiments with clustering points at the wall and boundary-layer edge showed no significant effect on stability results [19].

The code PSE-Chem is used to analyze the stability of the laminar mean-flow profiles. PSE-Chem uses the linear Parabolized Stability Equations coupled with the e^N method to predict transition. Details of the PSE can be found in Herbert [9], and the full derivation used in PSE-Chem is given by Johnson [17]. Linear stability theory is used to provide initial wavenumber guesses for the PSE marching using the global and local two-step procedure of Malik [22].

The disturbance equations are obtained from the Navier-Stokes equations by first decomposing the instantaneous flow into a mean and a fluctuating component, substituting into the Navier-Stokes equations, and subtracting the mean flow equations. The disturbance quantities are decomposed into a rapidly varying wave function and a slowly varying shape function, as shown in Equation 1.

$$\phi = \psi(x,y)e^{i(\int \alpha dx + \beta z - \omega t)} \qquad (1)$$

The shape function is parabolized, while all of the ellipticity is retained in the wave function.

Transition prediction is accomplished using the e^N method. The value e^N, where N is given by Equation 2, represents the total growth factor of a small amplitude initial disturbance.

$$N = \int_{\xi_o}^{\xi} \sigma d\xi \qquad (2)$$

In linear stability theory, only the contribution of $-\alpha_i$ is used to calculate N factors. In the PSE, the growth rate of the disturbances includes contributions from both the imaginary component of the streamwise wavenumber and the change in the kinetic energy of the shape function, as shown in Equations 3 and 4.

$$\sigma = -\alpha_i + \frac{1}{2E}\frac{dE}{d\xi} \qquad (3)$$

$$E = \int_{\Omega} \bar{\rho}(|\hat{u}|^2 + |\hat{v}|^2 + |\hat{w}|^2)d\xi \qquad (4)$$

Mack [8] showed that the disturbances can have several modes. The first mode is analogous to the TS waves of incompressible flow. The first mode is damped by wall cooling and is most amplified when it is at an oblique angle. The second mode can be thought of as a trapped acoustical wave. It is amplified by wall cooling, and it is most amplified when it is 2D. The higher modes always have lower amplification than the first or second mode, and they were not considered here.

3

Table 1: Test conditions for Stetson et al. [23] blunt cone experiment for all computations presented here.

Model Specifications	
Nose radius (mm)	3.81
Half angle	7°
Length (m)	1.016
Measured Flow Conditions	
M_∞	7.99
p_o (Pa)	4.0×10^6
T_o (K)	750
p_∞ (Pa)	410
Inferred Flow Conditions	
T_∞ (K)	54
ρ_∞ (kg/m^3)	0.0027
Re_∞/ft	2.5×10^6

SECOND MODE VERIFICATION: STETSON'S BLUNT CONE

The second mode calculations in STABL were verified by benchmarking against other codes since accurate experimental data were not available for validation. This exercise uncovered a number of issues, including bugs, alternative algorithms, and different transport property models. These discoveries led to changes that improved the quality of STABL. However, this was not an ideal situation, as many of the details of the other calculations are unknown. The methods used are not identical, as STABL uses the PSE and is designed for chemically reacting flows, whereas all of the benchmark codes use LST for perfect gas air flows. In addition, unknown errors may exist in the other codes or their useage that could account for differences in the results.

Experimental Conditions

The conditions chosen for the exercise were those of the blunt cone experiments of Stetson et al. [23] with the 3.81 mm nose radius. Stetson performed hot wire measurements in the boundary layer of a sphere-cone at zero degrees angle of attack and Mach 8 in Tunnel B at AEDC. The test conditions for all Stetson computations in this paper are summarized in Table 1. The freestream temperature and pressure are required inputs for STABL, and they were calculated from the specified flow conditions using the isentropic relations and the perfect gas law.

The Stetson et al. experiment has been analyzed by numerous other researchers using many different codes, which makes it an ideal benchmark for wind-tunnel conditions. Comparisons were made with results from References [24–32]. Most of these citations are summarized by Schneider [3].

Schneider [29] has shown that there are a number of open issues associated with this experiment. The axial station $s/r_n = 175$ is used for the vast majority of the computations presented in the literature. However, Stetson's data show considerable nonlinearity at this station which will not be captured by a LST analysis. Overshoots are present in the pitot pressure profiles, which are thought to be due to interference from the probe and have not appeared in any computation. Most researchers have assumed the wall is adiabatic, but the measured surface temperature is about 20% below the adiabatic temperature. The present work is not an attempt to resolve the discrepancies between computations and experiments. Rather, the intent is to replicate the computational results obtained with other codes to partially verify STABL. The large body of independent computational data makes this case ideal for verification, but these unresolved issues make complete validation from the experimental data impossible.

A number of issues were addressed to try to improve the agreement between the stability results of STABL and those of other researchers. Discussion of the laminar transport properties, freestream conditions, and grid generation will be given here. Robarge [19] describes other areas that were considered, including the method of boundary-layer edge detection, the wall temperature, the various options available in STABL, the compilers used, variable normalization, and the numerical behavior of PSE-Chem. These issues all had a smaller effect on the stability results.

Laminar Transport Properties

The laminar transport properties are an essential component of any numerical model. Accepted models exist for usage within normal ranges of temperature and pressure. However, there is considerable subjectivity in determining the best model for very high or low temperatures, and the best choice for one extreme is generally not the best choice for the other. Lyttle and Reed [33] showed for high temperatures that the transport properties employed can have a large impact on hypersonic stability results.

The components of STABL were designed primarily for high enthalpy air flows, such as those found in hypersonic flight or in shock tunnels. These flows are characterized by extremely high temper-

4

atures, causing dissociation, ionization, and chemical and thermal non-equilibrium, phenomena known collectively as real gas effects. Much more complicated flow models are required to accurately model these real gas effects than in situations where perfect gas behavior can be assumed. In contrast, the wind tunnel cases discussed here all have edge temperatures below 100 K. For the STABL suite to be valid in the low enthalpy regime, transport property models appropriate to that regime must be employed.

All of the computations cited previously were performed with a Sutherland viscosity law. Not all of the references provide details about the thermal conductivity modeling, but those that did specify the method assumed a perfect gas with a constant Prandtl number. It is probable that those who did not specify a method used this technique as well. Because all of the computations in the literature treated the air as a single gas rather than a mixture, none included the effects of diffusion. Due to the low temperatures involved, the production of monatomic species is negligible. The binary diffusion model should therefore not be a significant factor, and its accuracy was not investigated.

Viscosity

STABL originally used Blottner's [34] viscosity model for reacting flows to determine individual species viscosities [17]. This model uses empirical curve fits of the form given by Equation 5 to compute individual viscosities in kg/m-s for each species in the mixture.

$$\mu_s = 0.1 e^{(A_s ln(T) + B_s) ln(T) + C_s} \qquad (5)$$

The viscosity of the mixture is found by Wilke's semi-empirical mixing law.

Two sets of the coefficients A_s, B_s, and C_s are given in Table 2. The high temperature set is valid over the temperature range 1000 K–30000 K [34]. The low temperature set represents unpublished data provided by Blottner and is valid over the range 100 K–10000 K [35]. Values for the species NO, N, and O are given in Reference [34] and are the same for both temperature ranges. These species have mass fractions many orders of magnitude below those of N_2 and O_2 at wind tunnel temperatures, and their viscosity modeling was not investigated.

Figure 1 shows a comparison of the two methods given in Table 2 and the Sutherland law plotted with the experimental data of Grieser and Goldthwaite [36] and Matthews et al. [37]. The Blottner high temperature model is seen to differ greatly from the experimental data at low temperatures. At 80

Table 2: Blottner's Viscosity Curve Fit Coefficients

Coefficient	High Temp [34]	Low Temp [35]
A_{N_2}	0.0268142	0.0089993
B_{N_2}	0.3177838	0.6039338
C_{N_2}	-11.3155513	-12.4453814
A_{O_2}	0.044929	-0.0255541
B_{O_2}	-0.0826158	1.0503525
C_{O_2}	-9.2019475	-13.7080219

K, which is approximately the edge temperature for the Stetson case, the Blottner model overpredicts the viscosity by 70%. The Sutherland law diverges from the empirical models above approximately 1900 K, as is expected based on the approximations made in its derivation [38].

Based on this analysis, STABL was modified to incorporate different viscosity models for each temperature regime. STABL now uses the Sutherland law for low temperatures, the high temperature Blottner law for high temperatures, and the low temperature Blottner law for the intermediate range. Blending functions are used to ensure a smooth transition between the laws. The resulting method is shown as the STABL Blended curve in Figure 1. Agreement with the experimental data is considerably better.

It is important to note that none of the three laws implemented, including the Sutherland law, are necessarily accurate below 100 K. Several models exist for this low temperature regime. The Chapman-Enskog model [39] is based on the kinetic theory of gases and employs collision integrals to model the intermolecular forces. Keyes [40] and Maitland and Smith [41] both proposed empirical curve fits, and Mack [8] proposed a model hereafter referred to as the "Linear Sutherland Law" that is a linear extrapolation of the Sutherland Law below the Sutherland constant. Because the experimental data is so limited for this temperature range, there is no clear-cut choice for the best model to use. The Sutherland law was used for all computations in this work to provide consistency with the other computations referenced.

Thermal Conductivity

STABL calculates thermal conductivities for both translational and vibrational modes [17]. It uses Eucken's relation, given in Equations 6–8, to calculate the translational thermal conductivity of
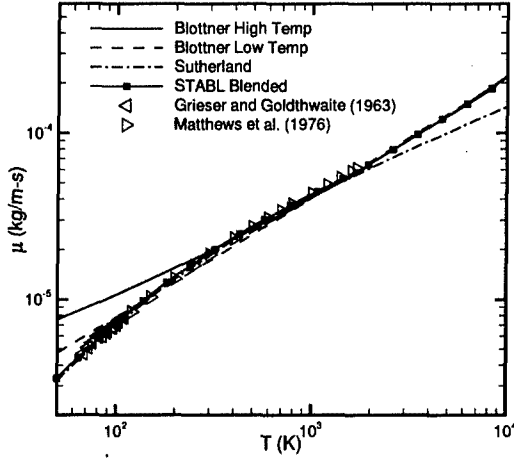
Figure 1: A comparison of the viscosity computed with both sets of coefficients of the Blottner form, the Sutherland law, and experimental data. The line labeled STABL Blended represents the modified method implemented as a result of the author's analysis.
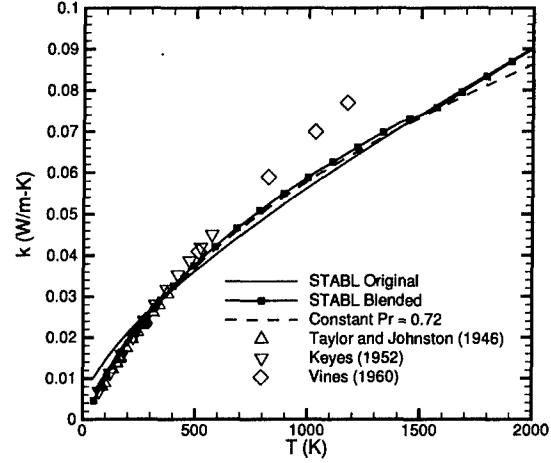

Figure 2: Thermal conductivity as computed by STABL before and after viscosity law modification and with a constant Prandtl number of 0.72 with constant specific heats and the Sutherland law. Experimental data are shown for reference.

each species.

$$k_s = \mu_s \left(\frac{5}{2} C_{v,tr_s} + C_{v,rot_s} \right) \qquad (6)$$

$$C_{v,tr_s} = \frac{3R}{2M_s} \qquad (7)$$

$$C_{v,rot_s} = \begin{cases} 0 & \text{monatomics} \\ \frac{R}{M_s} & \text{diatomics} \end{cases} \qquad (8)$$

The vibrational thermal conductivity is given by Equation 9.

$$k_{vib_s} = \mu_s C_{v,vib_s} = \mu_s \frac{de_{v_s}}{dT_v} \qquad (9)$$

The mixture thermal conductivities are computed with Wilke's semi-empirical mixing law.

Figure 2 shows a comparison of the thermal conductivity as computed by STABL and as computed using a constant Prandtl number of 0.72. The curve marked STABL Original uses the Blottner high temperature viscosity model, the curve marked STABL Blended uses the blended viscosity model described earlier, and the constant Prandtl number curve uses a Sutherland Law. Experimental data of Taylor and Johnston [42], Keyes [43], and Vines [44] are also presented. The STABL blended method agrees very

well at low temperatures with both the experimental data and the constant Prandtl number method. The use of the blended viscosity law causes the error in the calculated thermal conductivity with respect to the experimental data to drop from 70% to 4% at 80 K. However, all three of the methods differ significantly from the experimental data at higher temperatures. This may be due to the importance of the vibrational energy mode at higher temperatures, but this was not investigated further. Given the close agreement between the constant Prandtl number method and that used by STABL, this should not be a source of difference between STABL and the computational results of other researchers. However, it could have an impact on the accuracy of actual stability predictions.

Figure 3 shows the effect of the viscosity model on the amplification rate. The amplification curve peak is shifted from $(\omega \text{ kHz}, -\alpha_i \text{ 1/m}) = (136, 13.4)$ to $(132, 17.3)$, which is an increase in the peak amplification rate of 29% and a decrease of 3% in the frequency at which that occurs. The decrease in the frequency causes better agreement with the other researchers, but the increase in the amplification rate causes worse agreement. Although this improves agreement in the mean flow profiles, the agreement in the amplification curve is not improved by the change in the viscosity model.
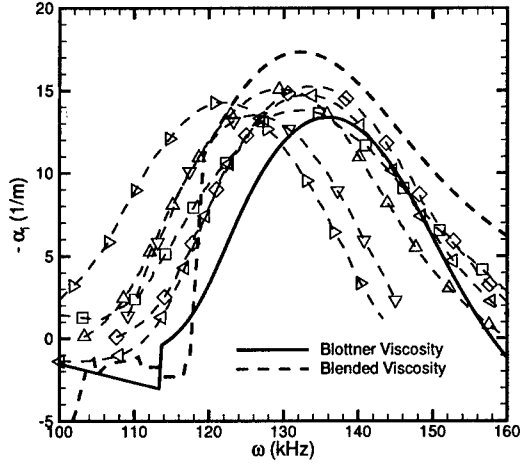
6

Figure 3: Amplification rate with the original and blended viscosity models for Stetson's blunt cone at $s/r_n = 175$ with $r_n = 3.81$ mm using the conditions given in Table 1.
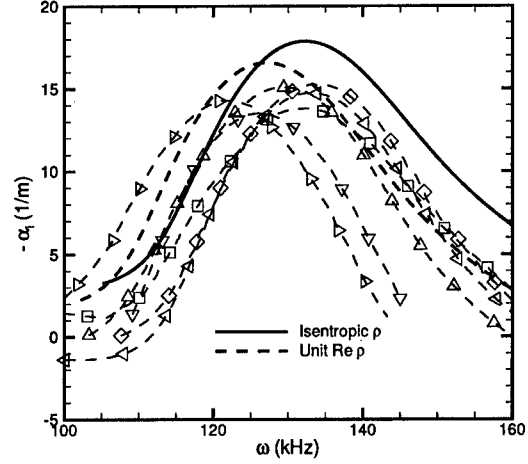

Figure 4: Amplification rates computed using two different values of freestream density for Stetson's blunt cone at $s/r_n = 175$ with $r_n = 3.81$ mm using the conditions given in Table 1.

Table 3: Unit Reynolds number for the Stetson et al. blunt cone experiment calculated using various viscosity models.

Viscosity Model	$\mu \left(\frac{kg}{m-s}\right)$	Re_∞/ft
Sutherland	3.546×10^{-6}	2.69×10^6
Linear Sutherland	3.771×10^{-6}	2.53×10^6
Keyes	3.893×10^{-6}	2.45×10^6
Chapman-Enskog	3.788×10^{-6}	2.53×10^6

Input Conditions

In Reference [23], Stetson et al. specify the quantities M_∞, P_o, T_o, P_∞, and unit Reynolds number. The Mach number, pressures, and stagnation temperature are measured quantities. The freestream temperature, which is a required input for many codes, including STABL, can be calculated using the isentropic relations. For this case, it is approximately 54.4 K. The unit Reynolds number is a derived quantity that depends on the viscosity model, which can be a source of uncertainty at that freestream temperature. Table 3 shows a comparison of the unit Reynolds number calculated using different viscosity laws in common use for the low temperature regime.

It seems likely that Stetson et al. used either the linear Sutherland law or the Chapman-Enskog model to calculate the unit Reynolds number they reported. However, the other researchers employed a standard Sutherland law for their computations, and the unit Reynolds number is an input condition for many CFD codes. To truly match the freestream conditions of Stetson's experiment using a Sutherland law code, a unit Reynolds number of $2.69 \times 10^6/ft$ would need to be used, rather than the $2.50 \times 10^6/ft$ specified in Reference [23].

The STABL mean flow solver uses the freestream temperature, freestream Mach number, and freestream density as input conditions. The freestream density is $0.02652\frac{kg}{m^3}$ when computed from the stagnation temperature and pressure using the perfect gas law and the isentropic relations. If a Sutherland viscosity law is used with a unit Reynolds number of $2.50 \times 10^6/ft$, the freestream density becomes $0.02464\frac{kg}{m^3}$. The first value appears to be more physically accurate, and should be used for comparison with the experimental data. However, the second number is most likely what was actually used in the other researchers' computations, and thus it should be used for code verification with the current benchmarks. Figure 4 shows the effect of changing the density input. Use of the unit Reynolds number based value shifts the amplification rate curve closer to the other researchers' results, moving the peak from (132,17.9) to (127,16.6).
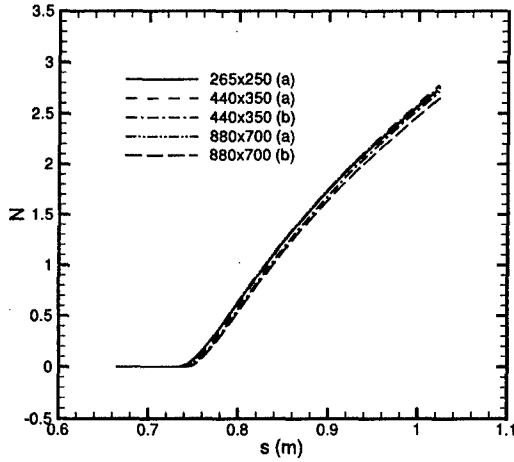
Figure 5: N factors computed using mean flows with varying grid resolutions for Stetson's blunt cone with $r_n = 3.81$ mm using the conditions given in Table 1.
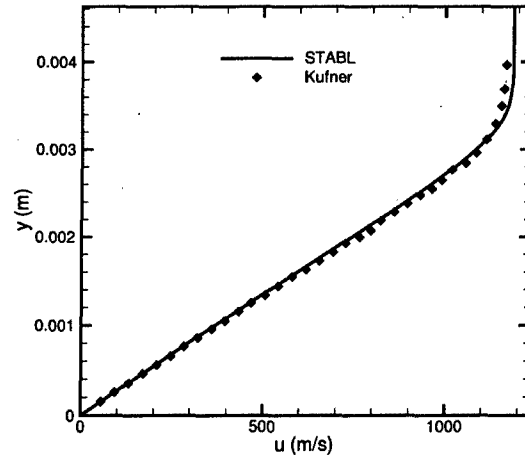

Figure 6: Mean velocity profile for conditions of Stetson et al. [23] at $s/r_n = 175$ with $r_n = 3.81$ mm compared with the results of Kufner et al. [26].

Grid Generation

The requirement for accurate second derivatives of the velocity and temperature profiles throughout the boundary-layer means that much finer grids must be used for stability analysis than for most other CFD applications. Figure 5 shows the N factors computed using several grids with varying resolution. The five curves shown used grids with 106, 121, 140, 239, and 276 points in the boundary-layer. The grids marked (b) in Figure 5 had an outer boundary that better matched the shock angle than those marked (a). The grids marked (b) produce slightly smaller N factors than the grids marked (a). There is no discernable trend with the total grid size. This suggests that the differences are due to the sensitivity of the stability calculations to small grid variations, and it cannot be conclusively said that one grid shape is better than the other. The scatter of approximately 5% at $s = 1.0$ m may represent an uncertainty in the results that cannot be eliminated through increasing mesh density. In any case, the differences are slight compared with the overall uncertainty associated with the use of the e^N method, and sufficient mesh spacing is used for the present results.

Results

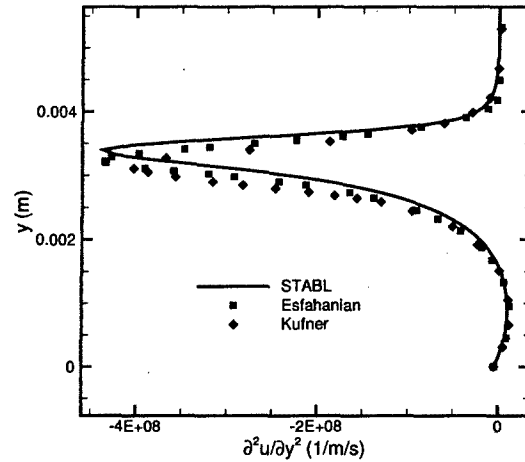The mesh used for the final computation contained 440 axial points and 350 body-normal points,

Figure 7: Second normal derivative of velocity profile for conditions of Stetson et al. [23] at $s/r_n = 175$ with $r_n = 3.81$ mm compared with the results of Kufner et al. [26] and Esfahanian [25].
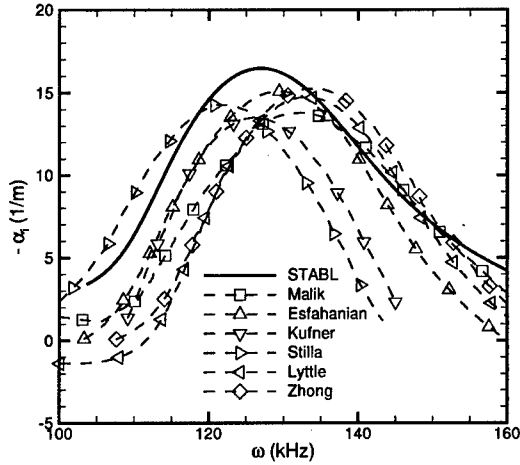
8

Figure 8: Amplification rate for conditions of Stetson et al. [23] at $s/r_n = 175$ with $r_n = 3.81$ mm.

Table 4: Location of the peak amplification as computed by STABL and several researchers.

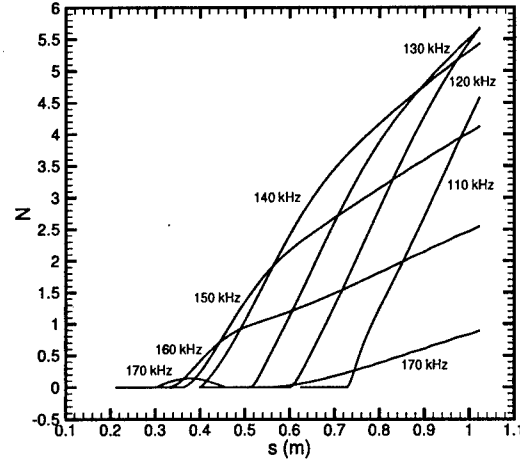| Computation	ω (kHz)	$-\alpha_i$ (1/m)
STABL	127	16.5
Malik [24]	132	13.8
Esfahanian [25]	129	15.1
Kufner [26]	126	13.5
Stilla [26]	122	14.3
Lyttle [31]	133	14.7
Zhong [32]	134	15.2

Figure 9: Maximum N factors obtained for various frequencies for the Stetson et al. blunt cone case with $r_n = 3.81$ mm.

and it corresponds to the 440x350 (b) line in Figure 5. Chemical and thermal nonequilibrium effects were modeled, and a freestream air mixture with standard mass fractions of 76.7% N_2 and 23.3% O_2 was assumed. The freestream density was set to $0.02464 \frac{kg}{m^3}$ to match the conditions of the other researchers. Thermal equilibrium was assumed in the freestream. STABL version 1.26 was used for both the mean flow and the stability calculations.

Figure 6 shows the mean tangential flow velocity at $s/r_n = 175$. Data in Figure 1a of Kufner et al. [26] was scanned and digitized and is plotted on Figure 6 for comparison. Agreement is generally good, although there is a small difference near the edge of the boundary-layer. Figure 7 shows the second derivative of the velocity profile with respect to the body-normal distance at the same station. Data from Figure 1b in Reference [26] is also plotted. Again, agreement is good except near the boundary-layer edge. Because the instabilities arise near the boundary-layer edge, these differences could be significant.

Figure 8 shows the amplification curve at $s/r_n = 175$ compared with that computed by other researchers. The peak frequency is slightly lower than the mean peak frequency, but it is within the scatter of the other results. The peak amplification rate is higher than any of the other researchers. The magnitude of the difference in the peak amplification rate is comparable to the scatter in the other

results shown. Table 4 summarizes the location of the peaks in Figure 8. A comparison with the results of Malik et al. [24] at $s/r_n = 215$ showed the same trends.

Figure 9 displays the maximum N factors obtained for various frequencies for the Stetson et al. blunt cone case. To obtain these N factors, a test matrix was constructed consisting of all combinations of the starting locations $s = 0.1, 0.15, \ldots, 1.0$ and frequencies $\omega = 50, 60, \ldots, 200$ kHz. PSE marching was conducted at each point in the test matrix, and the maximum N factors for each frequency are plotted in Figure 9. If, following the work of Malik et al. [24], Stilla [27], and Esfahanian and Hejranfar [30], transition is assumed to occur at $N = 5.5$ in this noisy environment, STABL

9

Table 5: Transition location predicted by STABL for Stetson et al. blunt cone case compared with that predicted by other researchers. Transition was assumed at N=5.5 for all computations.

Computation	s_{tr} (m)	$Re_{\infty,s_{tr}}$
STABL	1.00	8.192×10^6
Esfahanian PNS [30]	1.00	8.21×10^6
Esfahanian IPNS [30]	0.973	7.98×10^6
Stilla [27]	0.956	7.84×10^6
Malik et al. [24]	0.956	7.84×10^6
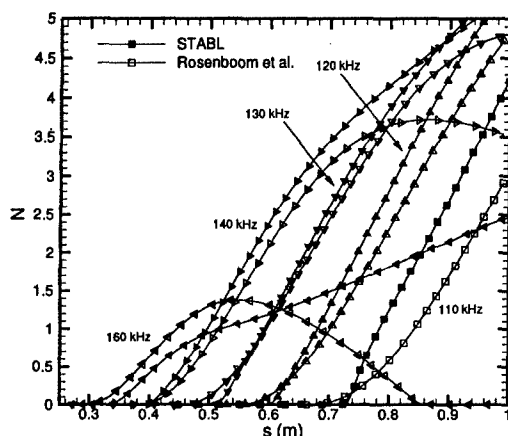
Figure 10: Comparison of N factors calculated by STABL with local N factors of Rosenboom et al. [28] for the Stetson et al. [23] case using the conditions given in Table 1.

would predict transition at $s = 1.00$ m with 130 kHz the most amplified frequency. Table 5 shows a comparison of the transition location predicted by STABL with that of the other researchers. The unit Reynolds number specified by Stetson et al. of 2.50×10^6/ft was used to convert between the $Re_{\infty,s_{tr}}$ and s_{tr}. Agreement with the other researchers is better than 5%.

Figure 10 shows a comparison of the N factors computed by STABL with the local N factors computed by Rosenboom et al. [28]. Agreement in the location of amplification of the various frequencies is fair, with no clear trends evident. The STABL 140 kHz and 160 kHz line show amplification throughout the full surface length, in contrast to the Rosenboom results, which begin to decay at $s = 0.85$ and

$s = 0.55$ m, respectively. The reason for the differences is not clear. The Rosenboom et al. results are not given in Table 5 because the data do not extend beyond $s = 1.00$ m or $N = 5.0$, but it is clear that the predicted transition location would be aft of $s = 1.00$ m.

FIRST MODE VERIFICATION

Sharp Cone at Mach 3.5

A sharp cone was analyzed using the conditions shown in Table 6 to verify STABL's ability to calculate first mode disturbances. The conditions correspond to experimental data obtained by Beckwith et al. [45] in the NASA Langley Mach 3.5 pilot quiet tunnel. This tunnel is designed to give freestream disturbance levels comparable to flight. The conditions chosen correspond to the fourth unit Reynolds number data set in Run 5 of Reference [45]. The first mode is expected to be dominant at this low freestream Mach number with an adiabatic wall.

This case was previously analyzed by Malik as case QT1 in Reference [46] using the COSAL stability code. This older LST-based code calculates temporal stability and uses Gaster's group velocity transformation to obtain spatial stability results. The mean flow was obtained from a boundary-layer code and provided as an input to COSAL.

Roger Kimmel [47] performed additional computations for this case using the e^{Malik} stability solver. This more recent code is also widely used for hypersonic stability analysis. Spatial stability results are calculated directly, and a perfect gas model is assumed. For the cases shown, the mean flow was provided by a similarity solver built into the e^{Malik} code. These computations were performed at the request of the author, and a good deal of collaboration and discussion with Dr. Kimmel occurred to troubleshoot differences between the results.

A grid with 450 axial points and 350 normal points was used for the DPLR2D mean flow solution. Exponential stretching was used in both directions to cluster grid points near the cone tip. This clustering increased the number of points within the boundary-layer and reduced the degree of numerical error caused by the discontinuity at the nose. The number of grid points within the boundary-layer varied from 148 near the nose tip to 109 at the base. Chemical and vibrational nonequilibrium effects were modeled with thermal equilibrium assumed in the freestream, and the blended viscosity model was used for all calculations.

Table 6: Test conditions for sharp cone at Mach 3.5

Condition	Value
Cone half angle	5°
Cone length (m)	0.381
Wall temperature	Adiabatic
M_∞	3.5
p_o (kPa)	525
T_o (K)	319.0
T_∞ (K)	92.53
ρ_∞ (kg/m^3)	0.02592
Re_∞/m	2.74×10^7
s_{tr} (m)	0.278

Figure 11: Mean flow velocity profiles for the sharp cone at Mach 3.5 at several axial locations.

Figure 11 shows wall-tangential mean flow velocity profiles computed by STABL and e^{Malik} at three axial locations. The profiles computed by STABL are slightly fuller than those computed by e^{Malik} for all distances. Figure 12 shows the mean temperature profiles for the same locations. Small but significant differences are seen at all three locations. These visible differences in the temperature and velocity can be expected to have a significant effect on the stability results. Meaningful second derivative comparisons were not available due to the lack of precision in the output of the e^{Malik} similarity solution.

Several mean flow solutions using different numbers of grid points within the boundary-layer were analyzed to ensure grid-independence of the solution. Figure 13 shows the effect of the different grids on the N factor calculations. These calculations are for a mode at $\omega = 104$ kHz and $\beta = 2400$/m with marching beginning at $s = 0.0339$ m. Four of the solutions are very similiar; the only difference is seen for the grid with 72 points in the boundary-layer. The reason for this repeatable difference is not clear. The grid with 109 points in the boundary-layer was used for all other calculations in this section.

To obtain the maximum N factors for this case, a test matrix was constructed consisting of $\omega = 25, 50, \ldots, 250$ kHz, $\beta = 1000, 2000, \ldots, 8000$ 1/m, and starting location $s = 0.02, 0.04, \ldots, 0.12$ m. All of the 480 combinations of these three parameters were analyzed in approximately 16 hours on two 2.4 GHz processors. The modes producing the maximum N factors at each location are shown in Figure 14. Amplification began at $s = 0.02$ m for the higher frequencies and shortly thereafter for the 75 kHz mode. At the experimental transition location of $s = 0.278$ m, the most amplified mode has a fre-
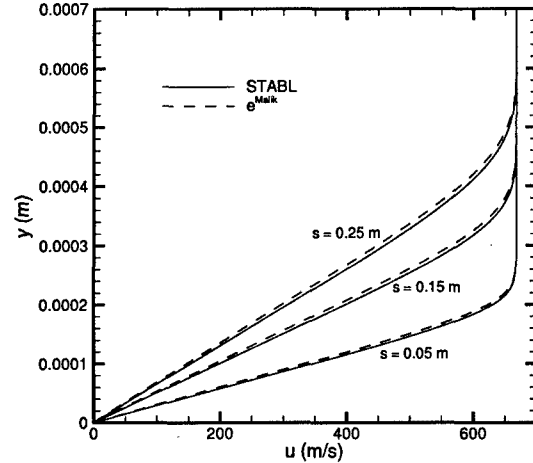
quency of 75 kHz, a β of 2000 1/m, and a N factor of 12.2. This N factor is larger than the range of 9–11 commonly calculated at experimentally measured transition locations in low disturbance environments.

Comparisons were made between the present results and those obtained by Malik using COSAL [46] and Kimmel using e^{Malik} [47]. Malik calculated N factor growth rates for six frequencies ranging from 22–188 kHz. His most amplified mode at the experimental transition location has a frequency of 78 kHz, a wave angle of approximately 60°, and a N factor of 10.1. Compared to the transition N factor calculated by STABL of 12.2, this is a significant difference, although the frequency and wave angle of the most amplified disturbances agree well.

Figure 15 shows a comparison of the N factors calculated by STABL and those calculated by Kimmel [47] using the e^{Malik} code for a mode at 104 kHz with $\beta = 2400$ 1/m. The N factors calculated by STABL are considerably higher than those calculated by e^{Malik}. The agreement is much worse than that seen in Figures 11 and 12 for the mean flow profiles. The difference in N factor may be due to the subtle differences in the mean flow, or it may be due to differences in the stability solvers. Plans for future work include using the mean flow generated by the similarity solver in e^{Malik} for stability calculations by PSE-Chem.
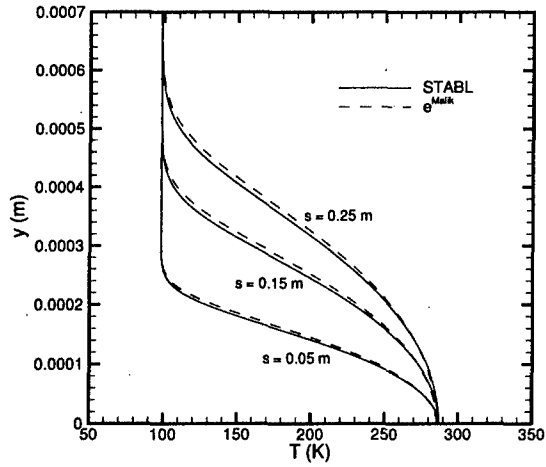
11

Figure 12: Mean flow temperature profiles for the sharp cone at Mach 3.5 at several axial locations.
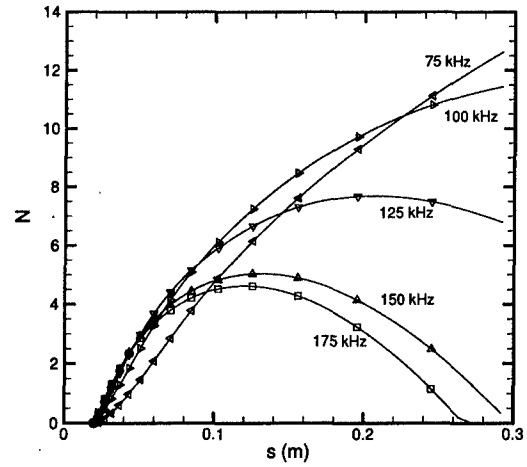

Figure 14: Maximum N factors obtained from many combinations of frequency, spanwise wavenumber, and starting location for the sharp cone at Mach 3.5.
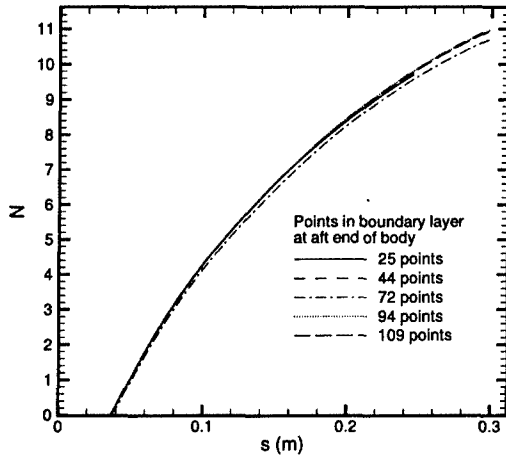

Figure 13: N factor calculations for the sharp cone at Mach 3.5 using five separate mean flow grids. Calculations are for a mode with $\omega = 104$ kHz and $\beta = 2400/m$, beginning at $s = 0.0339$ m.
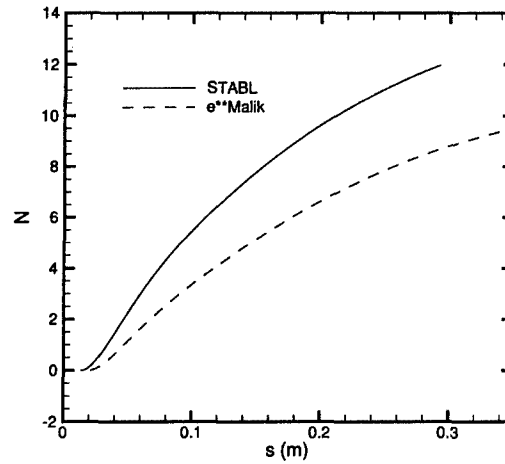

Figure 15: N factors calculated using STABL compared with results of Kimmel [47] using e^{Malik} for a mode at 104 kHz with $\beta = 2400$ 1/m for the sharp cone at Mach 3.5.

12

Table 7: Test conditions for cone with $r_n = 42.67$ mm at Mach 8

Condition	Value
Nose radius (mm)	42.67 mm
Cone half angle	7°
Maximum arc length (m)	11.35
Wall temperature	Adiabatic
M_∞	7.99
p_o (kPa)	4000
T_o (K)	750
T_∞ (K)	54
ρ_∞ (kg/m^3)	2.7×10^{-2}
Re_∞/m	2.5×10^6

Figure 16: First mode N factors for the large bluntness cone at Mach 8.

High Bluntness Cone at Mach 8

For a blunt cone, when the nose radius increases for a fixed, high freestream Mach number, the first mode may become dominant. For this reason, a very blunt cone was analyzed using the conditions shown in Table 7 to further verify first mode computations. The flow conditions match those of the Stetson et al. [23] blunt cone experiment, but the bluntness was increased while the ratio of the nose-tip radius to the body length was kept constant, making this case impractical for wind tunnel experiments. Rosenboom et al. [28,48] analyzed this case and found first mode N factor growth at a level comparable to second mode growth.

An accurate mean flow was computed using a mesh with 450 axial points and 350 wall-normal points. Approximately 100 grid points were contained within the boundary-layer over the cone frustum. The edge Mach number was approximately 4 near the cone shoulder and increased to approximately 6.3 far downstream of the nose.

Computations were performed with STABL to compare with the results of Rosenboom et al. Figure 16 shows samples of the first mode N factors calculated by STABL. A test matrix consisting of combinations of $s = 0.5, 1.0, \ldots, 10.5$ and $\beta = 20, 40, \ldots, 100$ 1/m was analyzed. Combinations involving additional values of $\beta < 20$ 1/m were also analyzed separately, but no significant amplification was found. For all cases shown, a frequency range of 1–10 kHz was analyzed at the starting location using LST, and the lowest unstable frequency was used for PSE marching. For these conditions, the marching frequency was always the lowest for which converged solutions could be obtained. β and $\ome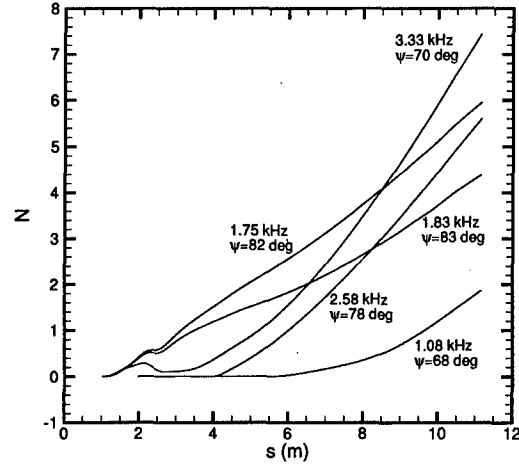ga$ were fixed as the marching progressed downstream. N= 5.5 is first reached at $s = 9.7$ m by a 3.33 kHz instability at 70°. Despite differences in the frequency and wave angle, the transition locations predicted by STABL and Rosenboom et al. agree extremely well. In addition, the general characteristics of the N factor curves calculated by STABL and Rosenboom et al. agree well. Both show an initial hump, followed by brief damping and a long rise. Table 8 summarizes the comparison.

Figure 17 shows the second mode N factor curves generated by STABL. A frequency range of 20–60 kHz was analyzed, but no eigenvalues were found by the global solver at frequencies greater than 35 kHz for any location. STABL selected the critical frequency at each starting location to begin PSE marching. Amplification begins at $s = 6.5$ m, slightly behind the critical location of $s = 5.5$ m calculated by Rosenboom et al. An N factor of 5.5 is first reached at $s = 9.0$ m by a 34 kHz wave. This is slightly ahead of the location calculated by Rosenboom of $s = 9.6$ m for the local calculation or $s = 9.8$ for the nonlocal calculation, but the difference is on the order of the starting distance resolution. Overall second mode agreement between STABL and Rosenboom is good. Table 8 summarizes the comparison.

An outstanding question in stability theory is the nature of the interaction between the first and second modes. Figure 18 shows the N factors for the most amplified first and second mode waves together with the edge Mach number distribution. The discontinuity in the edge Mach number at $s = 3$ m is
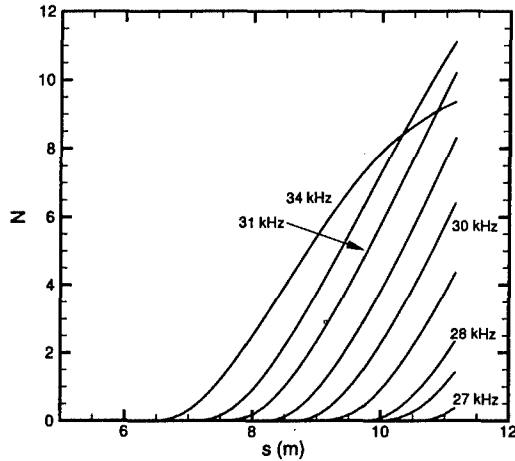
13

Figure 17: Second mode N factors for the large bluntness cone at Mach 8.

Table 8: Transition location predictions for the large bluntness cone. Transition is assumed at $N = 5.5$.

Computation	s_{tr} (m)	ω (kHz)	ψ
First Mode			
STABL	9.7	3.33	70°
Rosenboom [28,48]	9.7	2	70°
Second Mode			
STABL	9.0	34	0°
Rosenboom (local)	9.6	34	0°
Rosenboom (nonlocal)	9.8	34	0°

caused by numerical difficulties in defining the edge, as discussed further in Robarge [19]. The first mode amplifies over the full length of the body. The second mode begins to amplify when the edge Mach number is 5.7, and it becomes dominant when the edge Mach number is 6.0.

The calculations also showed another unstable mode that was not expected. Figure 19 shows the N factors calculated by two-dimensional waves at 1 kHz. The different curves represent different starting locations. The waves amplify very slightly until $s = $ 3 m, at which point they amplify very rapidly until $s = 4$ m. They then decay slightly until $s = 10$ m, at which point they again amplify rapidly until the end of the body. $N = 5.5$ is first reached at $s = 10.6$ m. These waves were found serendipitously
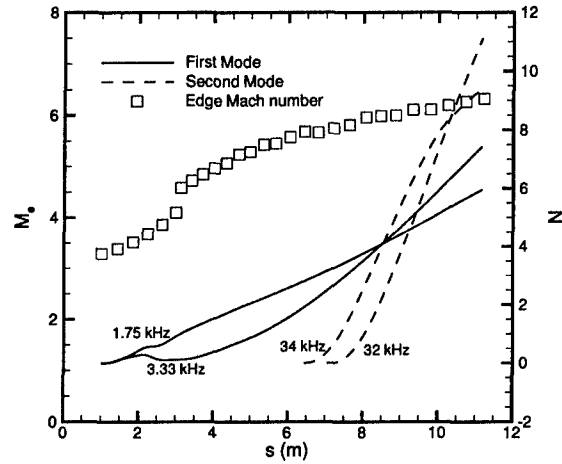

Figure 18: A comparison of the largest first and second mode N factors calculated by STABL for the large bluntness cone at Mach 8.
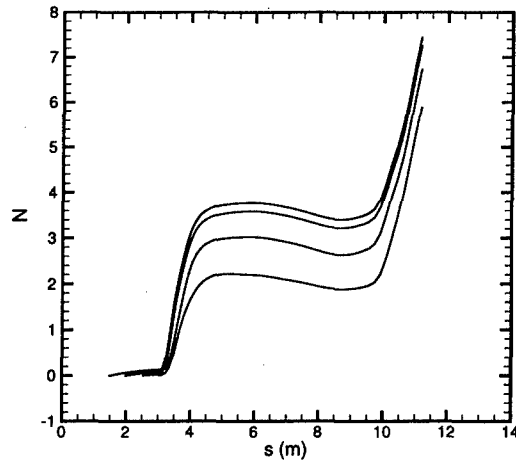

Figure 19: N factors of a two-dimensional instability at 1 kHz. The four lines represent different beginning marching locations.

14

during a search over the 1–10 kHz frequency range when the lowest amplified frequency was chosen for marching. Although this search was run every 0.5 m, only the starting locations between 1.5 and 3.0 m exhibited this behavior. The reason for the different amplification between the different starting locations is unknown. This might be a new phenomenon, but further investigation is necessary before it can be characterized.

CONCLUSIONS

Improved methods of hypersonic boundary-layer transition prediction require extensive verification and validation. Computations have been conducted using STABL for several benchmark cases.

The Stetson et al. [23] experiment is the best-known example of measured second mode wave growth on a blunt cone. This effort exposed the inadequacy of the method originally implemented in STABL for computing the viscosity of low temperature flows, such as those commonly found in hypersonic wind tunnels. Modifications that were made to use a blended viscosity law helped to extend the applicability of STABL to the low temperature regime. A related issue was the use of the proper freestream density. Many CFD codes require a unit Reynolds number input, but the unit Reynolds number reported in Stetson et al. is not consistent with the other reported quantities if a Sutherland viscosity law is used. Thus, any researcher that used the unit Reynolds number specified by Stetson et al. as an input to a code that uses the Sutherland law modeled the flow conditions of the experiment incorrectly.

Although the transition location predicted by STABL agreed well with that predicted by other researchers, there is considerable scatter in the amplification curves calculated for the 3.81 mm Stetson cone at $s/r_n = 175$. STABL calculates a peak amplification rate that is more unstable than any of the data sets used for comparison. However, the difference is approximately equal to the scatter in the other results. Furthermore, when the viscosity model and method of calculating the freestream density were changed, the results calculated by STABL shifted by amounts similar to the overall scatter in the results. This shows a high sensitivity to the physical models employed, and work should continue in validating these models for various flow regimes.

Computations were also conducted to verify the ability of STABL to predict first mode disturbances. A sharp cone at Mach 3.5 and a very blunt cone at Mach 8 were analyzed. The sharp cone compar-

ison showed good agreement in the transition location with the results of Malik [46]. However, the N factor computed for a single mode differed by 30% compared to a new corresponding calculation by the e^{Malik} code. Future plans call for the use of the mean flow solution produced by e^{Malik} in PSE-Chem stability calculations. This will help to localize the cause of the difference. Analysis of a large-bluntness cone showed first mode amplification over most of the body. Second mode amplification began farther aft, but it soon had greater total amplitude than the first mode. The predicted transition locations agreed well with the results of Rosenboom et al. [28] for both the first and second mode.

A great deal of progress has been made in transforming STABL from a research code to a design tool. The computations presented here help to provide confidence in the ability of STABL to analyze boundary-layer stability and predict transition. These results can also serve as a benchmark to allow other researchers using STABL to verify their method of operation. Additional computations on different cases in a variety of flow regimes should be performed to further this effort.

REFERENCES

[1] John J. Bertin and Russell M. Cummings. Fifty years of hypersonics: Where we've been, where we're going. *Progress in Aerospace Sciences*, 39:511–536, 2003.

[2] Air Force Space Command. Strategic master plan FY06 and beyond, October 2003.

[3] Steven P. Schneider. Hypersonic laminar-turbulent transition on circular cones and scramjet forebodies. *Progress in Aerospace Sciences*, 40(1):1–50, 2004.

[4] Steven P. Schneider. Flight data for boundary-layer transition at hypersonic and supersonic speeds. *Journal of Spacecraft and Rockets*, 36(1):8–20, January–February 1999.

[5] Eli Reshotko. Boundary layer instability, transition and control. Paper 94-0001, AIAA, January 1994.

[6] Steven P. Schneider. Effects of high-speed tunnel noise on laminar-turbulent transition. *Journal of Spacecraft and Rockets*, 38(3):323–333, May–June 2001.

[7] Steven P. Schneider, Craig Skoch, Shann Rufer, Erick Swanson, and Matthew P. Borg. Laminar-turbulent transition research in the Boeing/AFOSR Mach-6 Quiet Tunnel. Paper 2005-0888, AIAA, January 2005.

[8] Leslie M. Mack. Boundary-layer linear stability theory. In *AGARD Report 709, Special Course on Stability and Transition of Laminar Flow*, pages 3/1–3/81. AGARD, 1984.

[9] Thorwald Herbert. Parabolized stability equations. In *AGARD Report 793, Special Course on Progress in Transition Modeling*, pages 4/1–4/34. AGARD, 1993.

[10] Mujeeb R. Malik. Hypersonic flight transition data analysis using parabolized stability equations with chemistry effects. *Journal of Spacecraft and Rockets*, 40(3):332–344, May–June 2003.

[11] William L. Oberkampf and Frederick G. Blottner. Issues in computational fluid dynamics code verification and validation. *AIAA Journal*, 36(5):687–695, May 1998.

[12] Douglass E. Post and Lawrence G. Votta. Computational science demands a new paradigm. *Physics Today*, pages 35–41, January 2005.

[13] Frederick G. Blottner. Accurate Navier-Stokes results for the hypersonic flow over a spherical nosetip. *Journal of Spacecraft and Rockets*, 27(2):113–122, March–April 1990.

[14] Helen L. Reed. Computational fluid dynamics validation issues in transition modeling. *AIAA Journal*, 36(5):742–751, May 1998.

[15] Heath B. Johnson, Trevor G. Seipp, and Graham V. Candler. Numerical study of hypersonic reacting boundary layer transition on cones. *Physics of Fluids*, 10(10):2676–2685, Oct 1998.

[16] Heath B. Johnson and Graham V. Candler. PSE analysis of reacting hypersonic boundary layer transition. Paper 99-3793, AIAA, June 1999.

[17] Heath B. Johnson. *Thermochemical Interactions in Hypersonic Boundary Layer Stability*. PhD thesis, The University of Minnesota, 2000.

[18] Heath B. Johnson and Graham V. Candler. Hypersonic boundary layer stability analysis using PSE-Chem. Paper 2005-5023, AIAA, June 2005.

[19] Tyler W. Robarge. Computations of mean flows and instabilities on axisymmetric bodies at hypersonic speeds. Master's thesis, Purdue University, West Lafayette, Indiana, August 2005.

[20] Michael J. Wright, Graham V. Candler, and Deepak Bose. A data-parallel line relaxation method for the Navier- Stokes equations. Paper 97-2046, AIAA, June 1997.

[21] Robert W. MacCormack and Graham V. Candler. The solution of the Navier-Stokes equations using Gauss-Seidel line relaxation. *Computers and Fluids*, 17(1):135–150, 1989.

[22] Mujeeb R. Malik. Numerical methods for hypersonic boundary layer stability. *Journal of Computational Physics*, 86:376–413, February 1990.

[23] K.F. Stetson, E.R. Thompson, J.C. Donaldson, and L.G. Siler. Laminar boundary layer stability experiments on a cone at Mach 8, part 2: Blunt cone. Paper 84-0006, AIAA, January 1984.

[24] M.R. Malik, R.E. Spall, and C.-L. Chang. Effect of nose bluntness on boundary layer stability and transition. Paper 90-0112, AIAA, January 1990.

[25] Vahid Esfahanian. *Computation and Stability Analysis of Laminar Flow over a Blunt Cone in Hypersonic Flow*. PhD dissertation, The Ohio State University, 1991.

[26] Ewald Kufner, Uwe Dallmann, and Joachim Stilla. Instability of hypersonic flow past blunt cones — effects of mean flow variations. Paper 93-2983, AIAA, July 1993.

[27] J. Stilla. Engineering transition prediction for a hypersonic axisymmetric boundary layer.

AIAA Journal, 31(6):1358–1364, November 1994.

[28] I. Rosenboom, S. Hein, and U. Dallman. Influence of nose bluntness on boundary-layer instabilities in hypersonic cone flows. Paper 99-3591, AIAA, June 1999.

[29] Steven P. Schneider. Hypersonic laminar instability on round cones near zero angle of attack. Paper 2001-0206, AIAA, January 2001.

[30] Vahid Esfahanian and Kazem Hejranfar. Accuracy of parabolized Navier-Stokes schemes for stability analysis of hypersonic axisymmetric flows. *AIAA Journal*, 40(7):1311–1322, July 2002.

[31] Ian J. Lyttle, Helen L. Reed, Alexander N. Shipyluk, Anatoly A. Maslov, Dmitry A. Buntin, Eugene V. Burov, and Steven P. Schneider. Numerical-experimental comparisons of second-mode behavior for blunted cones. Paper 2004-0097, AIAA, January 2004.

[32] Xiaolin Zhong. Numerical simulation and experimental comparison of hypersonic boundary layer instability over a blunt cone. Paper 2004-2244, AIAA, June 2004.

[33] Ian J. Lyttle and Helen L. Reed. Sensitivity of second-mode linear stability to constitutive models within hypersonic flow. Paper 2005-0889, AIAA, January 2005.

[34] F.G. Blottner, M. Johnson, and M. Ellis. Chemically reacting viscous flow program for multicomponent gas mixtures. Technical Report SC-RR-70-754, Sandia National Laboratories, Albuquerque, NM, December 1971.

[35] Frederick G. Blottner. Personal communication, October 2004.

[36] Daniel R. Grieser and William H. Goldwaite. Experimental determination of the viscosity of air in the gaseous state at low temperatures and pressures. Technical Report AEDC-TDR-63-143, Arnold Engineering and Development Center, June 1963.

[37] G.P. Matthews, C.M.S.R. Thomas, A.N. Dufty, and E.B. Smith. Viscosities of oxygen and air over a wide range of temperatures. *Journal of the Chemical Society, Faraday Transactions I*, 72(1):238–244, January 1976.

[38] Frank M. White. *Viscous Fluid Flow*. McGraw Hill, Boston, 2nd edition, 1991.

[39] Sydney Chapman and T.G. Cowling. *The Mathematical Theory of Non-Uniform Gases*. Cambridge University Press, third edition, 1970.

[40] Frederick G. Keyes. A summary of viscosity and heat-conduction data for He, A, H_2, O_2, N_2, CO, CO_2, H_2O, and air. *Transactions of the ASME*, 73(5):589–596, July 1951.

[41] Geoffrey C. Maitland and E. Brian Smith. Critical reassessment of viscosities of 11 common gases. *Journal of Chemical and Engineering Data*, 17(2):150–156, February 1972.

[42] William J. Taylor and Herrick L. Johnston. An improved hot wire cell for accurate measurements of thermal conductivities of gases over a wide temperature range. *The Journal of Chemical Physics*, 14(4):219–233, April 1946.

[43] Frederick G. Keyes. The heat conductivity, viscosity, specific heat, and Prandtl numbers for thirteen gases. Technical Report 37, Project Squid, April 1952.

[44] Robert G. Vines. Measurement of the thermal conductivity of gases at high temperatures. *Transactions of the ASME: Journal of Heat Transfer*, 82(2):48–52, February 1960.

[45] Ivan E. Beckwith, Theodore R. Creel Jr., Fang-Jenq Chen, and James M. Kendall. Free stream noise and transition measurements in a Mach 3.5 pilot quiet tunnel. Paper 83-0042, AIAA, January 1983.

[46] Mujeeb R. Malik. Instability and transition in supersonic boundary layers. In E.M. Uram and H.E. Weber, editors, *Laminar-Turbulent Boundary Layers*, Proceedings of the Energy Sources Technology Conference, pages 139–147, New Orleans, LA, February 1984. ASME.

[47] Roger L. Kimmel. Personal communication, March–April 2005.

[48] I. Rosenboom, St. Hein, and U. Dallman. Numerische untersuchungen des einflusses der nasenstumpfheit auf grenzschichtinstabilitäten bei axialsymmetrischer kegelumströmung im hyperschall. Technical Report IB 223-98 A 34, Institut für Strömungsmechanik, DLR Göttingen, October 1998. (In German).

REPORT DOCUMENTATION PAGE	Form Approved OMB No. 0704-0188

Public reporting burden for this collection of information is estimated to average 1 hour per response, including the time for reviewing instructions, searching existing data sources, gathering and maintaining the data needed, and completing and reviewing the collection of information. Send comments regarding this burden estimate or any other aspect of this collection of information, including suggestions for reducing this burden, to Washington Headquarters Services, Directorate for Information Operations and Reports, 1215 Jefferson Davis Highway, Suite 1204, Arlington, VA 22202-4302, and to the Office of Management and Budget, Paperwork Reduction Project (0704-0188), Washington, DC 20503.

1. AGENCY USE ONLY *(Leave blank)*	2. REPORT DATE	3. REPORT TYPE AND DATES COVERED
	8.Jun.05	MAJOR REPORT

4. TITLE AND SUBTITLE
LAMINARY BOUNDARY-LAYER INSTABILITIES ON HYPERSONIC CONES:
COMPUTATIONS FOR BENCHMARK EXPERIMENTS.

5. FUNDING NUMBERS

6. AUTHOR(S)
1ST LT ROBARGE TYLER W

7. PERFORMING ORGANIZATION NAME(S) AND ADDRESS(ES)
PURDUE UNIVERSITY

8. PERFORMING ORGANIZATION REPORT NUMBER

CI04-1110

9. SPONSORING/MONITORING AGENCY NAME(S) AND ADDRESS(ES)
THE DEPARTMENT OF THE AIR FORCE
AFIT/CIA, BLDG 125
2950 P STREET
WPAFB OH 45433

10. SPONSORING/MONITORING AGENCY REPORT NUMBER

11. SUPPLEMENTARY NOTES

12a. DISTRIBUTION AVAILABILITY STATEMENT
Unlimited distribution
In Accordance With AFI 35-205/AFIT Sup 1

DISTRIBUTION STATEMENT A
Approved for Public Release
Distribution Unlimited

12b. DISTRIBUTION CODE

13. ABSTRACT *(Maximum 200 words)*

14. SUBJECT TERMS

15. NUMBER OF PAGES
17

16. PRICE CODE

17. SECURITY CLASSIFICATION OF REPORT	18. SECURITY CLASSIFICATION OF THIS PAGE	19. SECURITY CLASSIFICATION OF ABSTRACT	20. LIMITATION OF ABSTRACT